Nuclear Science and Techniques (2025) 36:84
https://doi.org/10.1007/s41365-025-01678-4

Sub-GeV events energy reconstruction with 3-inch PMTs in JUNO

Si-Yuan Zhang[1] · Yong-Bo Huang[1] · Miao He[2] · Cheng-Feng Yang[3] · Guo-Ming Chen[1]

Received: 26 January 2024 / Revised: 11 June 2024 / Accepted: 15 June 2024 / Published online: 20 March 2025

Abstract
A 20-kiloton liquid scintillator detector is under construction at the Jiangmen Underground Neutrino Observatory (JUNO) for several physics purposes. Detecting neutrinos released from nuclear reactors, the sun, supernova bursts, and Earth's atmosphere across a wide energy range necessitates efficient reconstruction algorithms. In this study, we introduce a novel method for reconstructing event energy by counting 3-inch photomultiplier tubes (PMTs) with or without signals. The proposed algorithm demonstrated excellent performance in accurate energy reconstruction, validated with electron Monte Carlo samples covering kinetic energies ranging from 10 MeV to 1 GeV.

Keywords Energy reconstruction · Liquid scintillator detectors · JUNO · OCCUPANCY method

1 Introduction

Liquid scintillator (LS) detectors are extensively used in nuclear and particle physics. Over the past few decades, LS detectors have played crucial roles in achieving remarkable scientific results in neutrino experiments [1–5]. The central detector (CD) of the Jiangmen Underground Neutrino Observatory (JUNO) will be the largest liquid scintillator detector in the world, aiming to probe multiple physics goals. One of the primary goals of the JUNO is to determine the mass ordering of neutrinos by accurately measuring and distinguishing tiny structural differences in the energy spectra of reactor neutrinos. Additionally, JUNO has a good potential for measuring neutrino oscillation parameters, supernova neutrinos, solar neutrinos, atmospheric neutrinos, and more. JUNO developed highly transparent LS and highly efficient photomultiplier tubes (PMTs) [6] with 78% photo coverage [7]. JUNO requires these designs to achieve the key requirements for determining neutrino mass ordering, including an unprecedented energy resolution of $3\%/\sqrt{E(\mathrm{MeV})}$ and better than 1% energy scale uncertainty. Additionally, JUNO has developed a dual calorimetry technique [8, 9] that can not only calibrate the nonlinearity of the charge response of 20-inch PMTs but also enables the detector to operate over a larger dynamic energy range.

Efficient algorithms are necessary to reconstruct individual event energies at the JUNO. In the LS, physics events deposit energy that is converted into photons that propagate and are detected by the PMTs. The type of particle and the magnitude and location of its energy deposition correspond to different hit patterns in the detector. Therefore, we can utilize hit information from the detector to reconstruct both the deposited energy and vertex of the particles and to identify their type. Typically, the energy is reconstructed based on the number of detectable photons, known as the visible energy (E_{vis}). Conversely, events can be classified as track-like (mainly muon-like events with long tracks in the detector) or cluster-like based on the topology of energy deposition in the detector. In addition, if a cluster is sufficiently small, it can be treated as a point-like event. The second moment S (Eq. 1) was introduced to describe the shapes of both point- and cluster-like events. This physical quantity

This work was supported by National Key R&D Program of China (No. 2023YFA1606103), National Natural Science Foundation of China (Nos. 12375105 and 12005044), and the Program of Bagui Scholars Program (XF).

✉ Yong-Bo Huang
huangyb@gxu.edu.cn

✉ Miao He
hem@ihep.ac.cn

[1] School of Physical Science and Technology, Guangxi University, Nanning 530004, China

[2] Institute of High Energy Physics, Beijing 100049, China

[3] School of Physics, Sun Yat-Sen University, Guangzhou 510275, China

is commonly used in collider experiments to describe the shapes of the clusters in energy calorimetry [10, 11].

$$S = \frac{\sum_{\alpha=1}^{N_E} E_\alpha \times [\vec{r_\alpha}(x_\alpha, y_\alpha, z_\alpha) - \vec{r}(x, y, z)]^2}{\sum_{\alpha=1}^{N_E} E_\alpha} \quad (1)$$

where N_E denotes the number of secondary energy depositions for the event. E_α and $\vec{r_\alpha}(x_\alpha, y_\alpha, z_\alpha)$ are the energy deposition and position in the α^{th} secondary energy deposition, respectively. $\vec{r}(x, y, z)$ is the energy-deposit center for the event, which is the weighted average of the secondary energy deposition and can be calculated as follows:

$$\vec{r}(x, y, z) = \frac{\sum_{\alpha=1}^{N_E} \vec{r_\alpha}(x_\alpha, y_\alpha, z_\alpha) \times E_\alpha}{\sum_{\alpha=1}^{N_E} E_\alpha} \quad (2)$$

Figure 1 compares the distributions of the second moment for electrons with different kinetic energies in the JUNO's LS. As the kinetic energy of the electrons increased, the distribution of the second moment became more diffused, indicating that it corresponded to a larger cluster of energy deposition. For comparison, Fig. 1 also shows the second-moment distribution of muons with different energies deposited in the LS. It can be observed that the second-moment distribution of the cluster- and track-like events with the same energy deposition is very different, which is related to their shape differences in energy deposition.

The basic idea of the current energy reconstruction algorithms in the JUNO central detector is based on either a data-driven maximum likelihood method (traditional method) or a machine learning strategy that utilizes information from the detector hit pattern. For example, reactor neutrinos ($\bar{\nu}_e$) are detected via inverse beta decay (IBD: $\bar{\nu}_e + p = e^+ + n$) in JUNO, the visible energy of this reaction is less than 10 MeV; JUNO has developed many robust reconstruction algorithms in this energy region based on traditional methods [12–14] or machine learning methods [15–17]. Events with visible energies larger than several hundred MeV in the detector are primarily due to atmospheric neutrino interactions, and their energy and direction reconstructions have been well studied using both the probabilistic unfolding method [18, 19] and machine learning technology [20–22] to assist in determining neutrino mass ordering [23]. However, energy reconstruction in the mid-energy region (10 MeV $< E_{\text{vis}} <$ several hundred MeV), which includes events from a diffuse supernova neutrino background (DSNB) [24], Michel electrons, low-energy atmospheric neutrinos, and possible proton decays [25], has rarely been discussed in previous studies.

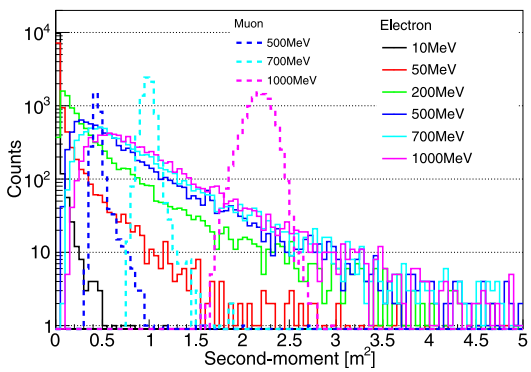

Fig. 1 (Color online) Distributions of the second moment for electrons with different kinetic energies

In general, the precise energy reconstruction in LS detectors faces several challenges:

(1) Precise PMT charge reconstruction. Because energy reconstruction primarily relies on the PMT charge information, any deviations in the PMT charge reconstruction will affect the accuracy of the energy measurement. In particular, the potential deviation of the reconstructed charge of the PMT (charge nonlinearity) is a crucial issue to consider for the energy reconstruction of high-energy events.
(2) Energy nonuniformity. Owing to the optical attenuation effect during the photon transmission process and the potential optical shielding effect caused by the mechanical structure of the detector and the PMT reception efficiency, the visible energy of the event is position-dependent.
(3) Event topology. Different reconstruction methods are typically required to handle track- and point- /cluster-like events separately.
(4) The impact of deviations in event tracks or the vertex/energy-deposit center on the energy reconstruction must be estimated.
(5) Energy leakage.

The data-driven maximum likelihood method has the advantage of better modeling of the response of a real detector. It primarily utilizes the detector response to radioactive sources as calibration templates, with the energy of radioactive sources being in the MeV range. A calibration map describing the dependence of visible energy on location can be constructed according to the calibration templates of the radioactive sources loaded at different locations of the detector. Consequently, the energy nonuniformity can be controlled to less than 1% [13]. Machine learning approaches, including convolutional neural networks (e.g., VGG and ResNet), have shown good performance in event reconstruction by effectively utilizing information from the detector response [15–17, 20–22]. However, it is crucial to

note that machine learning methods rely on a pure training sample from the data or simulation. A pure training sample from the data requires a reliable selection strategy and data accumulation, whereas the simulation usually requires adjustments according to the real data, especially in the early stages of detector operation.

In this study, we investigated the energy reconstruction of events spanning from MeV to GeV in the JUNO CD using the data-driven maximum likelihood method [14]. The data-driven maximum likelihood method and machine learning method in previous reconstruction algorithms have high requirements for the accuracy of PMT charge reconstruction, as mentioned earlier. We only utilized information of the PMT firing states (fired or unfired), known as the OCCUPANCY method to reduce the dependence on the accuracy and nonlinearity of the PMT charge reconstruction. The determination of the PMT firing states depends on the relationship between the PMT charge and the threshold. The fired state corresponds to the PMT charge equal to or greater than a certain threshold, whereas the unfired state corresponds to the PMT charge less than this threshold. This study focused on the reconstruction of cluster-like events because the calibration templates in this study were constructed using point-like (or cluster-like) calibration sources. Based on a study of event identification at JUNO [18], we can effectively distinguish cluster-like events from track-like events. The reconstruction of track-like events is also an important topic and was investigated in [18–22, 26–29]; however, it is not the subject of this study.

The details of our study are as follows. First, we introduce the JUNO detector and 3-inch PMT system (Sect. 2). We then present the methodology of our reconstruction (Sect. 3), including the construction of calibration maps and the construction of the maximum likelihood function. In Sect. 4, we show and compare the reconstruction performances. Finally, the summary is presented in Sect. 5.

2 JUNO detector and 3-inch PMT system

As shown in Fig. 2, JUNO mainly comprises three subdetectors: the CD, water Cherenkov detector, and top tracker detector [7, 30]. The CD consisted of 20 kilotons of LS and a 12 cm thick acrylic spherical container with a diameter of 35.4 m. The acrylic sphere is supported by a stainless steel-latticed shell through acrylic nodes and connecting bars. The primary component of the LS is linear alkyl benzene (LAB) with PPO (2.5-diphenyloxazole) as fluor and bis-MSB as the wavelength shifter. A total of 17612 20-inch PMTs (LPMTs) and 25600 3-inch PMTs (SPMTs) will be installed on the exterior of the container as photosensors to collect photon signals. Consequently, more than 1345 photoelectrons (PEs) will be observed by CD for a 1 MeV electron that fully

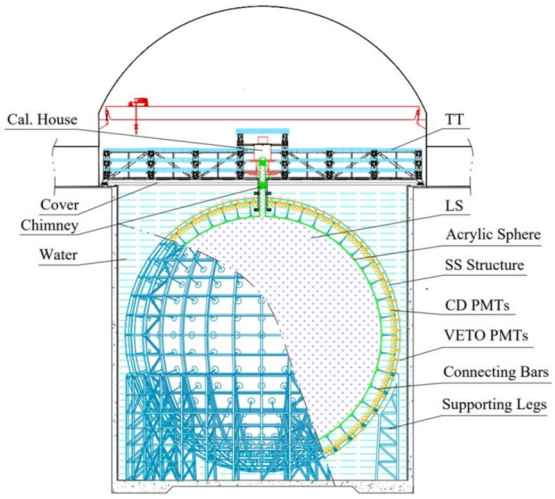

Fig. 2 A schematic view of the JUNO detector [7]

deposits its kinetic energy in the LS [7]. SPMTs will operate almost exclusively in the single photoelectron (spe) mode for reactor antineutrino detection ($E_{\text{vis}} < 10$ MeV). Therefore, SPMTs can serve as linear references for LPMTs and can be used to calibrate the charge nonlinearity of LPMTs. This feature is helpful in constraining some of the systematic uncertainties in LPMT energy reconstruction and improving the energy resolution. Moreover, SPMTs have the potential to detect supernova neutrinos and measure solar parameters (θ_{12} and Δm^2_{21}) independently [31].

For the detection of events with energies greater than tens of MeV or even GeV, most LPMTs receive tens or even hundreds of PEs. For example, Fig. 3a shows the distribution of the number of PEs (nPE) received by the LPMTs for 500 MeV electrons that deposit their kinetic energies in the LS. All the LPMTs were fired in this case. If energy deposition occurs at the edge of the detector, nearby LPMTs receive even more PEs. The linearity of the LPMT charge reconstruction over a large charge dynamic range is a challenge that requires calibration and validation in the future. Based on the experience with Daya Bay, an independent measurement system is an effective solution [32, 33]. In JUNO, the SPMT can be used to calibrate the nonlinearity in the charge reconstruction of the LPMT. For comparison, in the same case in which 500 MeV electrons deposited their kinetic energies in the LS, approximately 45%-60% of SPMTs were not triggered (Fig. 3c), and most of the fired SPMTs received fewer than 5 PEs (Fig. 3b) because their photocathode areas are approximately 40 times smaller. Therefore, we developed an energy reconstruction algorithm using only the information from SPMTs. In addition, the study in [34, 35] suggested that the readout electronics of JUNO SPMTs may also exhibit nonlinearity when receiving multiple hits. To minimize this effect, we used only the firing

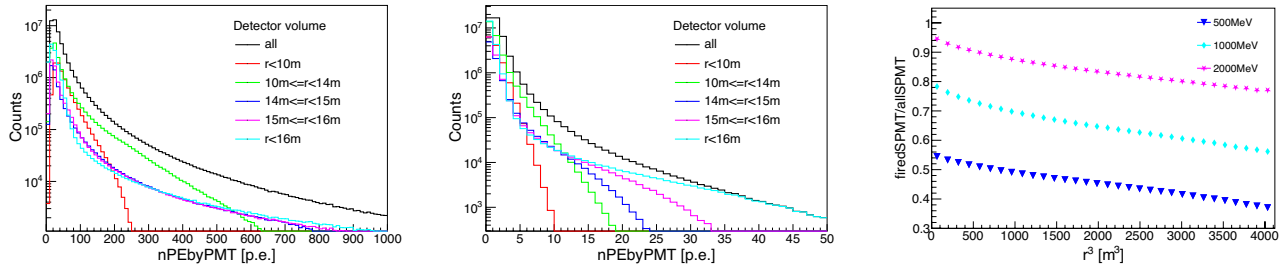

Fig. 3 The distribution of nPE received by LPMTs **a** and SPMTs **b** for 500 MeV electrons deposited their kinetic energies in the LS. **c** The proportion of fired SPMTs for electrons deposited their kinetic energies at different locations

information (fired or unfired). Further details are provided in Sec. 3

The JUNO detector is currently under construction. To investigate the performance of our reconstruction, Monte Carlo (MC) simulation data generated by the JUNO offline software [36–40] was utilized. The software is based on the Geant4 toolkit [41–43] and the software for non-collider physics experiments (SNiPER) framework [44]. In the simulation, a realistic detector geometry, comprehensive physical interaction processes, scintillation processes, and optical transmission processes were employed. The optical parameters of the LS were implemented based on precise measurements [45–52]. Furthermore, we incorporated official electronic simulations that include SPMT's charge smearing, transit time spread, and dark noise, which are referenced in the measurement [53, 54]). In this study, both the calibration and validation samples were generated based on MC simulations with identical configurations.

3 Method of energy reconstruction

3.1 The probabilities of SPMT's firing states

For each SPMT, the number of detected PEs obeys a Poisson distribution as follows:

$$\text{Poisson}(k_i|\mu_i) = \frac{e^{-\mu_i} \times {\mu_i}^{k_i}}{k_i!}, \tag{3}$$

where k_i is the nPE detected by the i^{th} SPMT and μ_i is its expected mean value. As mentioned above, to reduce the dependence on the charge reconstruction accuracy, the OCCUPANCY method was applied, which uses only the information from SMPT's firing states (fired or unfired). Therefore, only two states of k_i should be considered: $k_i = 0$ (unfired) and $k_i > 0$ (fired). The probabilities of these two states are described by Eqs. (4) and (5) [55, 56].

$$P_{\text{unfired}}(\mu_i) = \text{Poisson}(k_i = 0|\mu_i) = e^{-\mu_i} \tag{4}$$

$$\begin{aligned} P_{\text{fired}}(\mu_i) &= \text{Poisson}(k_i > 0|\mu_i) \\ &= 1 - P_{\text{unfired}}(\mu_i) = 1 - e^{-\mu_i} \end{aligned} \tag{5}$$

In real detection, k_i is smeared by fluctuations in the photoelectron detection, whereas μ_i is distorted because of the additional contribution from the PMT dark count. In addition, thresholds must be applied to each SPMT to avoid false triggering due to electronic noise; this also affects the observation of μ_i. In general, 0.3 PEs is chosen as the typical threshold because it can effectively handle electronic noise. Considering these effects, the probabilities of the unfired and fired states are:

$$\begin{aligned} P_{\text{unfired}}(\mu_i^{\text{true}}) &= P(q_i < q_i^{\text{threshold}}|\mu_i^{\text{true}}) \\ &= \text{Poisson}(k_i = 0|\mu_i^{\text{true}}) + P_{\text{threLoss}}(\mu_i^{\text{true}}), \\ P_{\text{fired}}(\mu_i^{\text{true}}) &= P(q_i \geq q_i^{\text{threshold}}|\mu_i^{\text{true}}) \\ &= 1 - P_{\text{unfired}}(\mu_i^{\text{true}}) \end{aligned} \tag{6}$$

where q_i is the reconstructed charge of the i^{th} SPMT, μ_i^{true} ($\mu_i^{\text{true}} = \mu_i^{\text{phy}} + \mu_i^{\text{dn}}$) is the mean value of the Poisson distribution, which consists of two components:

(1) μ_i^{phy} caused by the visible energy of physics events.
(2) μ_i^{dn} introduced by the dark count (DR_i) of the i^{th} SPMT, which can be calculated using $\mu_i^{\text{dn}} = \text{DR}_i \times t$ in the time window of t.

$P_{\text{threLoss}}(\mu_i^{\text{true}})$ is the probability of $q_i < q_i^{\text{threshold}}$ (0.3 PEs in this study) for $k_i > 0$, and is calculated as follows:

$$\begin{aligned} &P_{\text{threLoss}}(\mu_i^{\text{true}}) \\ &= \sum_{k_i=1}^{n} [\text{Poisson}(k_i|\mu_i^{\text{true}}) \times \int_0^{q_i^{\text{threshold}}} \text{Gaus}(q_i|g_i, \sigma(g_i))\, dq_i] \end{aligned} \tag{7}$$

where $g_i = S_i^{\text{gain}} \times k_i$ and $\sigma(g_i) = \sqrt{g_i} \times \sigma_i^{\text{spe}}$, with n indicates the case of multiple PEs, S_i^{gain} corresponds to the ratio between the real SPMT gain and the normal SPMT gain (3×10^6) in JUNO, σ_i^{spe} denotes spe resolution of the i^{th} SPMT. In real detection, S_i^{gain}, σ_i^{spe}, and DR_i can be obtained from PMT calibration.

3.2 Construction of the calibration map

JUNO designed a comprehensive calibration system [7] to understand the detector response by deploying multiple radioactive sources in various locations inside/outside the CD, including the Auto Calibration Unit (ACU), Cable Loop System (CLS), Guide Tube Calibration System (GTCS), and Remotely Operated Vehicle (ROV). Figure 4, shows the individual calibration systems in the CD and their scanning regions. For example, the ACU system scans the detector response along the central axis with multiple calibration sources, and the CLS system can scan in a 2-dimensional plane (X-Z plane) with multiple calibration sources using the central and side cables. The strategy of the JUNO calibration system was developed and optimized based on the Monte Carlo simulation results [57].

In energy reconstruction, μ_i^{phy} directly corresponds to the visible energy of an event in the detector, which is the basis of energy reconstruction in our method. Assuming that a calibration source is loaded at location $\vec{r}(r, \theta, \phi = 0)$ in the central detector, the mean value of the visible energy-induced PEs for the i^{th} SPMT is $\mu_i^{\text{phy\_source}}$, which corresponds to the visible energy (denoted as E^{source}) of the calibration source. Subsequently, for an event that deposits energy at the same location, the relationship between the event's visible energy E_{vis} and μ_i^{phy} for the i^{th} SPMT can be described as follows:

$$\mu_i^{\text{phy}} = \frac{E_{\text{vis}}}{E^{\text{source}}} \times \mu_i^{\text{phy\_source}} \tag{8}$$

It should be noted that μ_i^{phy} is not only related to the visible energy and position of the event, but also to the relative position (θ_{SPMT}) of the event and the i^{th} SPMT. This relationship can be determined using calibration data by constructing a calibration map. In Sect. 3.3, the maximum likelihood method was adopted to reconstruct the visible energy by estimating μ_i^{phy} using the calibration map and invoking the firing states of 25600 SPMTs from the data. Next, the construction of the calibration map is introduced.

Based on the calibration strategy of JUNO [57], this study used the ^{68}Ge source (positron source, with $E^{\text{source}} = 1.022$ MeV) to calibrate the X-Z plane with assistance from both the ACU and CLS systems across 227 positions. Using the JUNO offline software [36–40], 10000 ^{68}Ge events were generated for each calibration location on the X-Z calibration plane. During the calibration, when the ^{68}Ge source is loaded at one of the 227 planned locations [58], the probability of the unfired state for the i^{th} SPMT can be estimated using Eq. (9), where $N_{q_i < q_i^{\text{threshold}}}$ is the number of events with $q_i < q_i^{\text{threshold}}$, N_{total} is the total number of events for the calibration sample, and $N_{\text{total}} = 10000$. Similarly to Eq. (6), we can derive the relationship between the observable quantities $P_{\text{unfired}}(\mu_i^{\text{true\_source}})$ and $\mu_i^{\text{true\_source}}$ (corresponding to the visible energy) in Eq. (10) for conversion during the subsequent reconstruction. In addition, for convenience, we introduce an intermediate variable $\mu_i^{\text{det\_source}}$ (the effective mean value of the detected PEs) for the i^{th} SPMT in Eq. (10) based on the mathematical form of Eq. (4). This functional form helps provide a more intuitive understanding of how PMT dark counts and the threshold effect impact $\mu_i^{\text{true\_source}}$. Subsequently, $\mu_i^{\text{det\_source}}$ is estimated using Eq. (11) using the calibration data. This calculation requires that the i^{th} SPMT is not fired for all 10000 events in the calibration sample (^{68}Ge); otherwise, this method is no longer applicable. The above extreme scenario is extremely unlikely because of the low visible energy of ^{68}Ge, and the fact that even the most marginal of the 227 calibration positions is approximately 2 m away from its neighboring SPMTs.

$$\begin{aligned} P_{\text{unfired}}(\mu_i^{\text{true\_source}}) &= P(q_i < q_i^{\text{threshold}} | \mu_i^{\text{true\_source}}) \\ &= \frac{N_{q_i < q_i^{\text{threshold}}}}{N_{\text{total}}} \end{aligned} \tag{9}$$

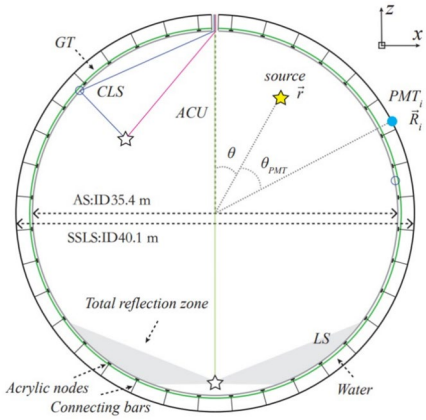

Fig. 4 The individual calibration systems in the CD and their scanning regions [13]

$$P_{\text{unfired}}(\mu_i^{\text{true\_source}}) = \text{Poisson}(k_i = 0|\mu_i^{\text{true\_source}}) + P_{\text{threLoss}}(\mu_i^{\text{true\_source}}) \quad (10)$$
$$\overset{\text{def}}{=} e^{-\mu_i^{\text{det\_source}}}$$

$$\mu_i^{\text{det\_source}} = -\ln P_{\text{unfired}}(\mu_i^{\text{true\_source}}) = -\ln \frac{N_{q_i<q_i^{\text{threshold}}}}{N_{\text{total}}} \quad (11)$$

Note that $\mu_i^{\text{phy\_source}}$ is the value required for energy reconstruction (Eq. 8), whereas $\mu_i^{\text{det\_source}}$ includes contributions from visible energy, PMT dark counts, charge smearing, and the threshold effect. According to Eqs. (6), (10) and PMT parameters (S_i^{gain}, σ_i^{spe} and DR_i) from PMT calibration, we can find the relationship between $\mu_i^{\text{phy\_source}}$ and $\mu_i^{\text{det\_source}}$. Figure 5 shows an example of an SPMT with an spe resolution and dark count rate of 30% and 1 kHz, respectively. The readout window was 1000 ns. It appears that dark counts dominate $\mu_i^{\text{det\_source}}$ for small $\mu_i^{\text{phy\_source}}$, whereas the combined effect of the dark count, smearing, and threshold remains stable at approximately 2% for the given setting as $\mu_i^{\text{phy\_source}}$ increases.

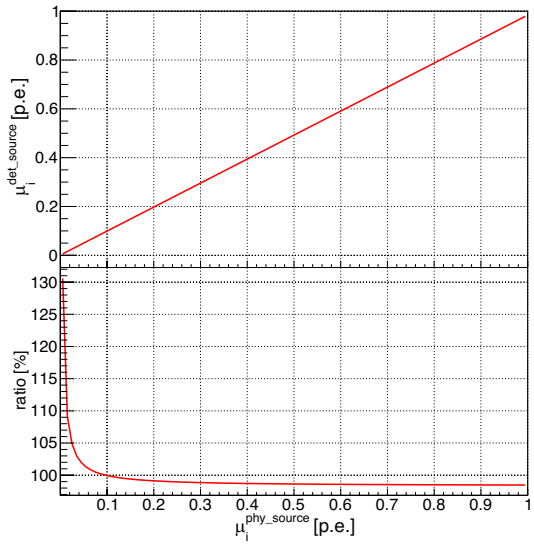

Fig. 5 The relationship between $\mu_i^{\text{det\_source}}$ and $\mu_i^{\text{phy\_source}}$ for an SPMT with an spe resolution and dark count rate of 30% and 1 kHz, respectively; and the readout window is set to 1000 ns. The bottom panel shows the ratio of $\mu_i^{\text{det\_source}}/\mu_i^{\text{phy\_source}}$

Considering that the CD has good symmetry and the SPMTs with the same relative position with respect to the calibration source exhibit similar responses, to enhance the accuracy, we further group and combine SPMTs with similar θ_{SPMT} values in the calculation of $\mu_i^{\text{phy\_source}}$. In this study, θ_{SPMT} was divided into 1440 groups from 0° to 180° with 0.125° per group. This approach was successfully verified and applied in [14]. Therefore, SPMTs in the same θ_{SPMT} group have similar values of $\mu_i^{\text{phy\_source}}$ for each ^{68}Ge source location $\vec{r}(r, \theta, \phi = 0)$, the average of which is denoted as $\mu^{\text{phy\_source}}(\vec{r}, \theta_{\text{SPMT}})$. The calibration map can be constructed after ^{68}Ge scans 227 locations on the X-Z plane and all $\mu^{\text{phy\_source}}(\vec{r}, \theta_{\text{SPMT}})$ calculated. Considering the calibration performance and time consumption in JUNO, only approximately 227 calibration points were available in the current calibration strategy. Therefore, it was necessary to apply interpolation to the remaining positions. Figure 6a and b show examples of the calibration maps before and after interpolation, respectively.

The following is a brief summary of the main steps involved in constructing the calibration map.

(1) For ^{68}Ge loading at location $\vec{r}(r, \theta, \phi = 0)$, calculate the effective mean value of the detected PEs ($\mu_i^{\text{det\_source}}$) for each SPMTs using Eq. (11).

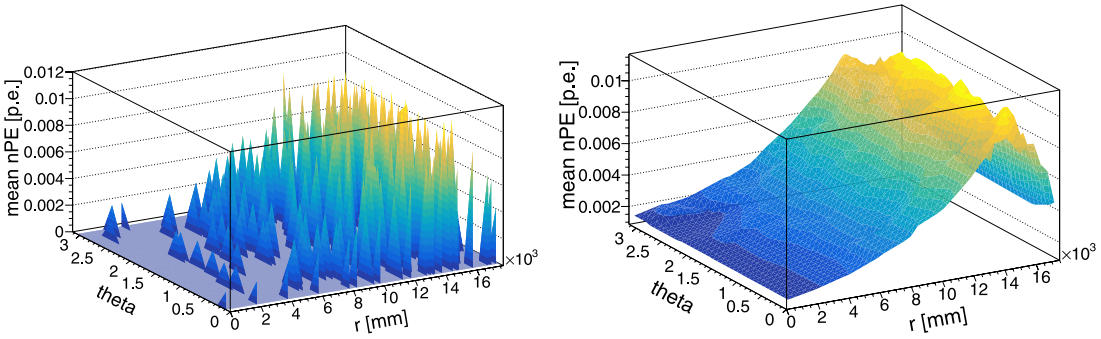

Fig. 6 (Color online) Example of calibration map for one θ_{SPMT} group whose θ_{SPMT} values from 18° to 18.125°. **a** θ_{SPMT} in [18°,18.125°); **b** θ_{SPMT} in [18°,18.125°)

(2) Calculate $\mu_i^{\text{phy\_source}}$ by correcting PMT dark counts and threshold effect, Fig. 5 shows an example of the relationship between $\mu_i^{\text{det\_source}}$ and $\mu_i^{\text{phy\_source}}$ for an SPMT.
(3) Calculate $\mu^{\text{phy\_source}}(\vec{r}, \theta_{\text{SPMT}})$, which is the average value of $\mu_i^{\text{phy\_source}}$ for each θ_{SPMT} group.
(4) Repeat the above steps for the calibration data at all locations.
(5) Apply interpolation to the remaining positions.
(6) For a given ^{68}Ge location $\vec{r}(r, \theta, \phi = 0)$, the $\mu^{\text{phy\_source}}(\vec{r}, \theta_{\text{SPMT}})$ value corresponding to each SPMTs can be obtained.

The calibration map was generated using the calibration data on the X-Z plane ($\phi = 0$) by considering that the detector exhibits good symmetry along the ϕ direction [57]. Based on the detailed study in [13], the ϕ symmetry is reliable for events located within 16 m. However, considering that the acrylic sphere is supported by a stainless steel-latticed shell through acrylic nodes and connecting bars, the dependence on ϕ near the edge cannot be ignored anymore due to the shadowing effect caused by the numerous acrylic nodes. In the future, the ϕ symmetry needs to be checked and validated using real data, which can be corrected if necessary.

3.3 Construction of maximum likelihood function

To reconstruct the visible energy of a cluster-like event whose energy-deposit center is known in the detector, a likelihood function can be constructed as follows:

$$\mathcal{L} = \prod_{i=1}^{N_{\text{unfired}}} P_{\text{unfired}}(\mu_i^{\text{phy}}) \prod_{i=1}^{N_{\text{fired}}} P_{\text{fired}}(\mu_i^{\text{phy}}) \tag{12}$$

where $N = N_{\text{unfired}} + N_{\text{fired}} = 25600$, N_{unfired} and N_{fired} correspond to the number of SPMTs with $q_i < 0.3$ PEs and $q_i \geq 0.3$ PEs, respectively. $P_{\text{unfired}}(\mu_i^{\text{phy}})$ and $P_{\text{fired}}(\mu_i^{\text{phy}})$ are the probabilities of the unfired and fired states, respectively, and can be calculated using Eq. (6). In the calculation, μ_i^{phy} of each SPMT can be estimated by considering the relationship in Eq. (8) and invoking the $\mu^{\text{phy\_source}}(\vec{r}, \theta_{\text{SPMT}})$ value from the calibration map. In addition, the differences in quantum efficiency (QE) between individual SPMTs in the same θ_{SPMT} group should be considered [59]. Consequently, $\mu_i^{\text{phy\_source}}$ of the i^{th} SPMT needs a correction that can be calculated as follows:

$$\mu_i^{\text{phy\_source}} = \frac{QE_i}{\frac{1}{m}\sum_{j=0}^{m} QE_j} \times \mu^{\text{phy\_source}}(\vec{r}, \theta_{\text{SPMT}}) \tag{13}$$

where m is the number of SPMTs in the θ_{SPMT} group classified by the θ_{SPMT} value, and QE_j is the QE of the j^{th} SPMT in this group.

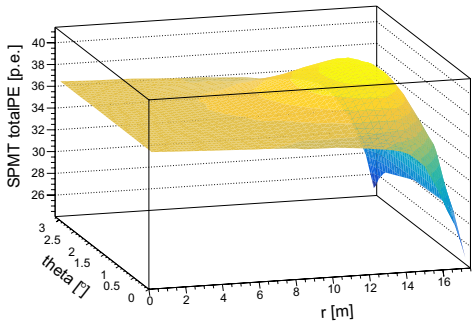

Fig. 7 (Color online) The total number of PEs observed by 25600 SPMTs for ^{68}Ge source located at different positions

Next, the ROOT's minimization class TMinuit2Minimizer [60–62] is used to minimize $-\ln\mathcal{L}$. In the minimization, the visible energy E_{vis} of the cluster-like event (whose energy-deposit center is known and the parameter to be determined is introduced in Sect. 4.1); its initial value (E_{initial}) can be estimated using Eq. (14) using the total number of PEs (totalPE) of all the SPMTs to reduce the reconstruction time. totalPE$^{\text{source}}(r)$ is totalPE observed by 25600 SPMTs for the ^{68}Ge source located at different positions (Fig. 7). Comparing the value of totalPE$^{\text{source}}(r)$ at the center of the CD and around $r = 15$ m, there is approximately 7% nonuniformity introduced by the reception of PMTs and the optical attenuation effect in the process of photon transmission. A decreasing radius larger than ~15.6 m was primarily caused by the total reflection and shadowing effects.

$$E_{\text{initial}} = \frac{\text{totalPE}(r)}{\text{totalPE}^{\text{source}}(r)} \times E^{\text{source}} \tag{14}$$

After minimization, TMinuit returns the predicted visible energy value as a result of energy reconstruction. Furthermore, the response difference caused by the spatial scale of the energy deposition is investigated in Sect. 3.4, and it was found that it had little influence on the analysis.

3.4 Comparison of cluster-like event and point-like event

^{68}Ge was used as the positron source. The positron annihilated in the source capsule (stainless steel + PTFE) with a pair of 0.511 MeV γs emitted. Most of the energy of γs is deposited within ~30 cm in the LS; therefore, ^{68}Ge is not strictly a point-like source but a cluster-like source similar to the high-energy electrons described in Sect. 1. In [13], it was found that accurate energy reconstruction below 10 MeV can be affected by the cluster size of the energy deposition. In this study, we constructed a calibration map using the approximate point-like ^{68}Ge source (cluster size in ~30 cm) to determine the location-dependent $\mu_i^{\text{phy\_source}}$ from calibration data and carry out energy reconstruction. Therefore, it is necessary

to investigate whether this calibration map can be applied to higher energy electrons with larger cluster sizes (up to several meters) by assuming that they are point-like events with their energy-deposit centers as the event positions.

According to Eq. (8), $\mu_i^{\rm phy}$ can be calculated for an event with a known position in the LS with $E^{\rm source}$ and $\mu_i^{\rm phy\_source}$ obtained from the calibration map. In the energy reconstruction, our algorithm assumes that all energy deposition is equivalent to those occurring at the energy-deposit center. However, in real detection, $\mu_i^{\rm phy}$ of the $i^{\rm th}$ SPMTs are contributed by the cumulative effect of each secondary energy deposition. $\mu_i^{\rm phy}$ was adopted using different strategies to estimate the potential bias caused by the spatial scale of energy deposition for high-energy events. As shown in Eqs. (15) and (16), they were calculated as point- and cluster-like events, respectively.

$$\mu_i^{\rm phy}|_{\rm point-like} = \frac{1}{E^{\rm source}} \times \sum_{\alpha=1}^{N_E} E_\alpha \times \mu_i^{\rm phy\_source}(\vec{r}) \tag{15}$$

$$\mu_i^{\rm phy}|_{\rm cluster-like} = \frac{1}{E^{\rm source}} \times \sum_{\alpha=1}^{N_E} E_\alpha \times \mu_i^{\rm phy\_source}(\vec{r_\alpha}) \tag{16}$$

The official simulation software of JUNO was used to generate electron samples with different kinetic energies, and the details of each secondary energy deposition (E_α and $\vec{r_\alpha}$) were recorded to calculate Eqs. (15) and (16). As shown in Eq. (17), the sum of all SPMT's $\mu_i^{\rm phy}$ is directly proportional to the visible energy of the event. Therefore, any bias present in the sum of all SPMT's $\mu_i^{\rm phy}$ indicates a deviation in the visible energy. We compared the calculation results of the different strategies, as shown in Eq. (18) and Fig. 8. It was found that the ratio approaches 1 with an increase in r^3, and has a small bias ($\leq 0.5\%$) at the edge for electrons with kinetic energies larger than 200 MeV. This result indicates that our algorithm and reconstruction strategy are applicable to the energy reconstruction of high-energy events with large spatial scales of energy deposition.

$$\sum_{i=1}^{N} \mu_i^{\rm phy} = \frac{E_{\rm vis}}{E^{\rm source}} \times \sum_{i=1}^{N} \mu_i^{\rm phy\_source} \tag{17}$$

$$Ratio = \frac{\sum_{i=1}^{N} \mu_i^{\rm phy}|_{\rm cluster-like}}{\sum_{i=1}^{N} \mu_i^{\rm phy}|_{\rm point-like}} \tag{18}$$

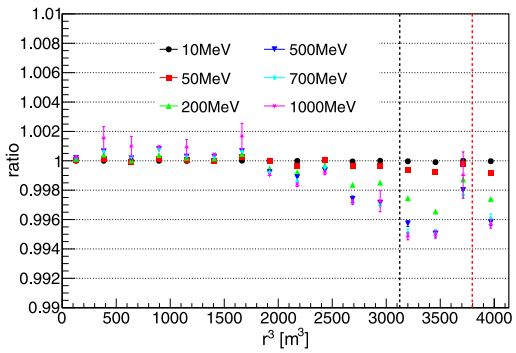

Fig. 8 Comparison between the calculation results of point-like and cluster-like treatment. The ratio, defined in Eq. (18), was found to be close to 1 for electron samples with different kinetic energies at various positions. On this plot, the black vertical dotted line corresponds to $r = 14.6$ m, and the red vertical dotted line ($r = 15.6$ m) corresponds to the boundary of the total reflection region, which is caused by the larger refractive index of the LS (which has a similar refractive index to the Acrylic) than water

4 Reconstruction result

In this section, the JUNO offline software was used to simulate electrons uniformly distributed in the CD with different kinetic energies (10, 20, 50, 100, 200, 350, 500, 700, 1000, and 2000 MeV) as the MC sample to validate the reconstruction algorithm. The MC samples were generated after a full-chain simulation at JUNO. A 16 m radius cut was applied to avoid energy leakage for high-energy events and the total reflection effect at the edge of the detector. Finally, approximately 10000 events exist for each electron sample.

4.1 Reconstruction of energy-deposit center

As introduced in Sect. 3.3, the energy-deposit center of the event is required to reconstruct the visible energy. Therefore, before energy reconstruction, it is necessary to reconstruct the energy-deposit center. The energy-deposit center reconstruction of high-energy cluster-like events faces greater dispersion compared with the vertex reconstruction of point-like events (Sect. 1). After the investigation, it was found that the time-based algorithm developed and verified by [63] was suitable and could be applied to our analysis.

The time-based algorithm uses the distribution of the time-of-flight (t.o.f.) corrected time Δt (Eq. 19) of an event to reconstruct its vertex and t_0 (event time). The principle of the time-based algorithm is that the Δt distribution is independent of the event vertex after applying time-of-flight correction. In this study, we applied it to the reconstruction of an energy-deposit center.

$$\Delta t_i = t_i - \text{t.o.f.}_i \tag{19}$$

In Eq. 19, t_i is the first hit time of the $i^{\rm th}$ SPMT, and t.o.f._i is the time of flight from the energy-deposit center to the $i^{\rm th}$ SPMT. In the calculation of t.o.f._i, the optical path length includes both the length in the LS and in water. Subsequently, a correction vector was constructed and minimized

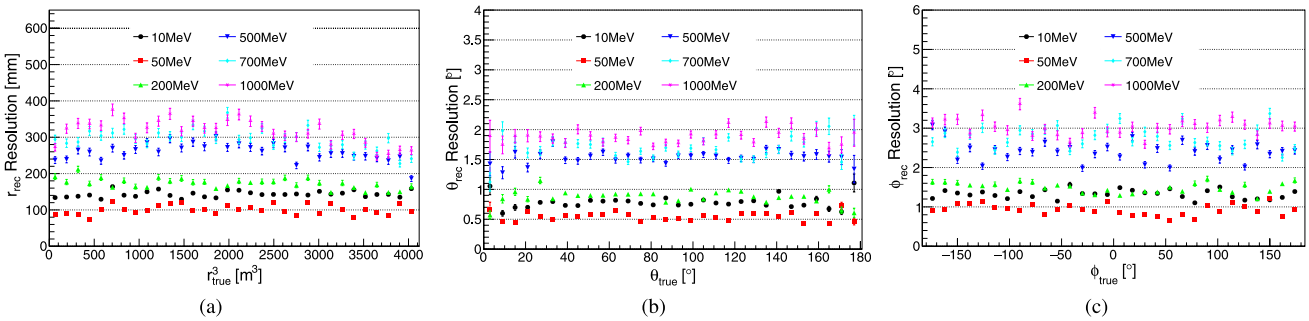

(a) (b) (c)

Fig. 9 Reconstruction resolution of electron's energy-deposit center. **a** Reconstruction resolution of r; **b** Reconstruction resolution of θ; **c** Reconstruction resolution of ϕ

by iterating the energy-deposit center. Further details are provided in [63]. Finally, the reconstructed energy-deposit center can be obtained, and Figs. 15 and 9 show the performance. The reconstruction biases of θ (Fig. 15b) and ϕ (Fig. 15c) remain small and stable as the energy increases, whereas the reconstruction bias of r (Fig. 15a) gradually increases with the energy. However, it could still be controlled to within 150 mm at 1 GeV. This bias is still acceptable considering that the cluster size could be several meters for a 1 GeV electron. The effect of the deviation on the energy reconstruction will be discussed later. However, the reconstruction bias of r tends to decrease at the edge of the detector compared to other regions, mainly because of energy leakage near the edge, especially for high-energy events.

In Fig. 9, it can be observed that the reconstruction resolutions of r, θ and ϕ increase with electron energy between 50 MeV and 1 GeV. For example, the resolutions of r, θ and ϕ were approximately 100 mm, 0.5°, and 1.0° for 50 MeV electrons, respectively, whereas the resolutions of r, θ and ϕ were approximately 340 mm, 1.8°, and 3.0° for 1 GeV electrons, respectively. This effect is primarily due to the greater dispersion of the energy deposition of high-energy electrons. The resolutions of 10 MeV electrons are slightly larger than that of 50 MeV electrons. This is because the hit number of the SPMTs is small (~400 PEs for 10 MeV),

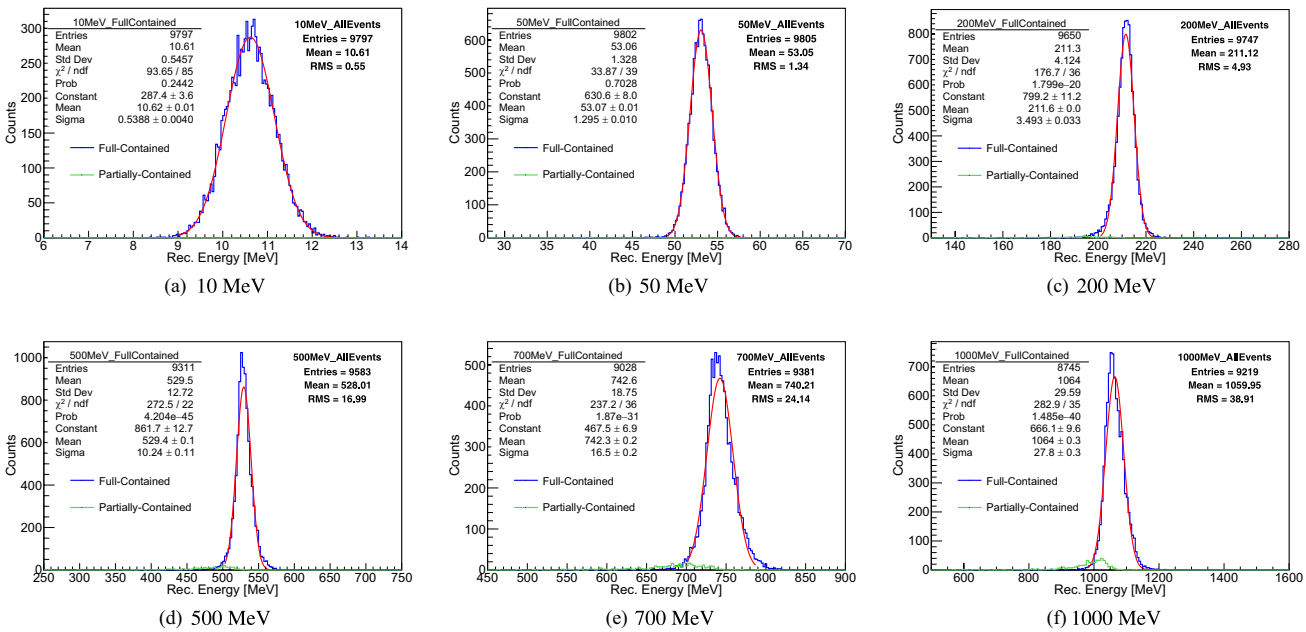

(a) 10 MeV (b) 50 MeV (c) 200 MeV

(d) 500 MeV (e) 700 MeV (f) 1000 MeV

Fig. 10 Discrete energy reconstruction with reconstructed edep vertex after electronic simulation and charge reconstruction. The blue line is the FC events, and the green line is the PC events. According to the fitting results (red line) of FC spectra, it can be observed that the reconstructed visible energy is about 6% larger than the deposited energy of the electron. More specifically, for electrons with kinetic energies of 10 MeV, 50 MeV, 200 MeV, 500 MeV, 700 MeV, and 1 GeV, the ratio of reconstructed visible energy to deposited energy is found to be 1.062, 1.061, 1.058, 1.059, 1.060, and 1.064, respectively. The corresponding explanation is provided in the text

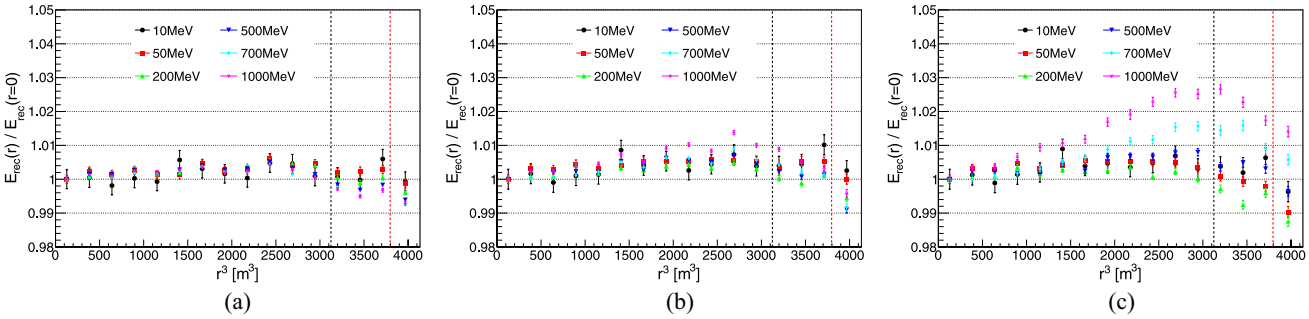

Fig. 11 Uniformity of discrete energy reconstruction for FC events. On each plot, black vertical dotted lines correspond to $r = 14.6$ m, and red vertical dotted lines ($r = 15.6$ m) correspond to the boundary of the total reflection region, which is caused by a larger refractive index of the LS (which has a similar refractive index to the acrylic) than water. **a** Without electronic simulation and charge reconstruction, using true energy-deposit center for energy reconstruction; **b** With electronic simulation and charge reconstruction, using true energy-deposit center for energy reconstruction; **c** With electronic simulation and charge reconstruction, using reconstructed energy-deposit center for energy reconstruction

and less information is available for reconstruction using the time-based algorithm.

4.2 Energy reconstruction performance

Next, the performance of energy reconstruction is introduced. The reconstructed energy spectra of the electrons with different kinetic energies are shown in Fig. 10. The blue spectra correspond to events whose energies were fully contained (FC) in the LS, whereas the green spectra correspond to events whose energies were partially contained (PC) in the LS. For electrons with energies greater than 500 MeV, the proportion of PC events increased, and the 16 m cut cannot completely exclude the case of energy leakage. The FC spectra could be fitted well with a Gaussian function, and the reconstructed energy was approximately 6% higher than the deposited energy of the electron. According to the official simulation in JUNO, when anchored at the 2.223 MeV gamma peak generated by (n, γ)H, high-energy electrons exhibit an energy nonlinearity of ~6% [64]. Thus, this deviation is understood to be mainly caused by the energy nonlinearity response of the LS. Conversely, the nonuniformity of the energy reconstruction may also introduce some small deviations, but generally, less than 1%, as shown in Fig. 11c.

To understand the nonuniformity shown in Fig. 11c, a and b can be compared, which corresponds to the cases using true energy-deposit center without/with electronic simulation and charge reconstruction. In Fig. 11a, for electron samples with different energies, the nonuniformity is consistent at about 0.5% from the center of the detector to the edge. After the electronic simulation and charge reconstruction (Fig. 11b), there is a slight increase in nonuniformity, but it still remains within 1.5%. Figure 11c corresponds to the case using reconstructed energy-deposit center that shows deviation (Fig. 15), as a result, for 500 MeV and 1 GeV electrons, their energy nonuniform are about 2% and 3% at the edge. Furthermore, when PC events were included (Fig. 12), they mainly affected the nonuniformity of high-energy electrons located in the edge region.

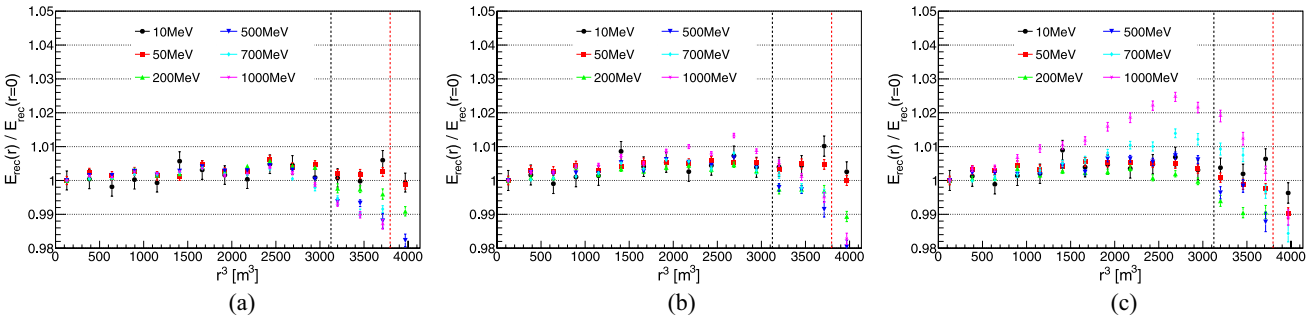

Fig. 12 Uniformity of discrete energy reconstruction for all (FC+PC) events. On each plot, black vertical dotted lines correspond to $r = 14.6$ m, and red vertical dotted lines ($r = 15.6$ m) correspond to the boundary of the total reflection region, which is caused by a larger refractive index of the LS (which has a similar refractive index to the acrylic) than water. **a** Without electronic simulation and charge reconstruction, using true energy-deposit center for energy reconstruction; **b** With electronic simulation and charge reconstruction, using true energy-deposit center for energy reconstruction; **c** With electronic simulation and charge reconstruction, using reconstructed energy-deposit center for energy reconstruction

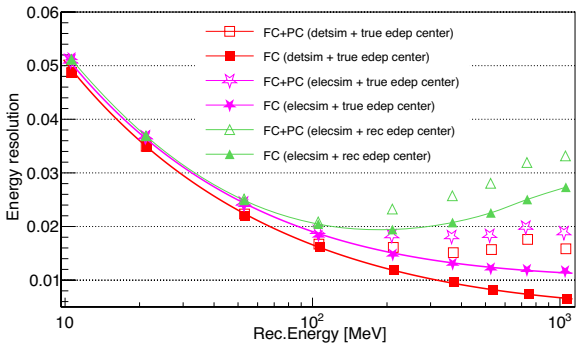

Fig. 13 Resolution in several discrete energies in simulation phase. The red squares correspond to the resolution in the detector simulation. The pink stars and the green triangles correspond to the resolution after electronic simulation and charge reconstruction. The energy reconstructions of the red squares and pink stars use the true center of energy deposition, while the green triangles utilize the reconstructed center for their energy reconstruction. The energy reconstruction of the red squares and the pink stars uses the true energy-deposit center, while the energy reconstruction of the green triangles uses the reconstructed energy-deposit center. On the other hand, solid and hollow are used to mark the FC events and FC+PC events, respectively

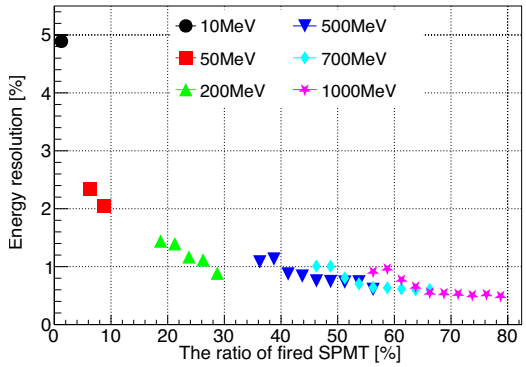

Fig. 14 The resolution varies with the fired ratio of SPMT at different energies

Figure 13 shows the energy resolution performance. The solid points correspond to the reconstruction results of the FC events, whereas the hollow points include both FC events and PC events. The red squares and pink stars denote the cases using the true energy-deposit center for energy reconstruction, whereas the green triangles denote the reconstructed energy-deposit center. In addition, electronic simulation, and charge reconstruction were applied to the reconstruction results shown by the pink stars and green triangles. Comparing energy resolutions in different conditions, it can be found that the energy reconstruction performance of the high-energy events is good using the OCCUPANCY strategy, and the energy resolution is about 0.8% for 1 GeV electrons in the ideal case (red solid squares). In a more realistic situation, by including electronic simulation and charge reconstruction, the resolution is only approximately 0.3% worse, indicating that the correction works well in controlling the influence of the PMT dark count and threshold effect. From the comparison of solid points and hollow points, the PC events mainly affect the electrons whose kinetic energy is larger than 100 MeV, and their energy resolutions deteriorate by approximately 1%. In real detection, the reconstructed energy-deposit center is required for energy reconstruction, and its smearing introduces additional smearing on the reconstructed energy, especially for high-energy electrons. Consequently, the energy resolution was approximately 3.2% for 1 GeV electrons based on our algorithm. In Fig. 14, the relationship between the energy resolution and the fired ratio of the SPMT is investigated using an electron sample without electronics simulation, and a true energy-deposit center was applied. In general, a higher fired ratio of the SPMT corresponds to a better energy resolution. This indicates that our algorithm has the potential to be applied to higher energy events when the fired ratio of the SPMT is not close to 1 but must solve the problem of energy-deposit center reconstruction, which has a larger bias at higher energies.

To apply the algorithm to the experiment, we need to consider how to perform performance validation in the future, especially given the lack of calibration sources in the hundreds of MeV range, which is a common challenge in the validation of high-energy event reconstruction. First, we can select calibration samples in the tens of MeV range

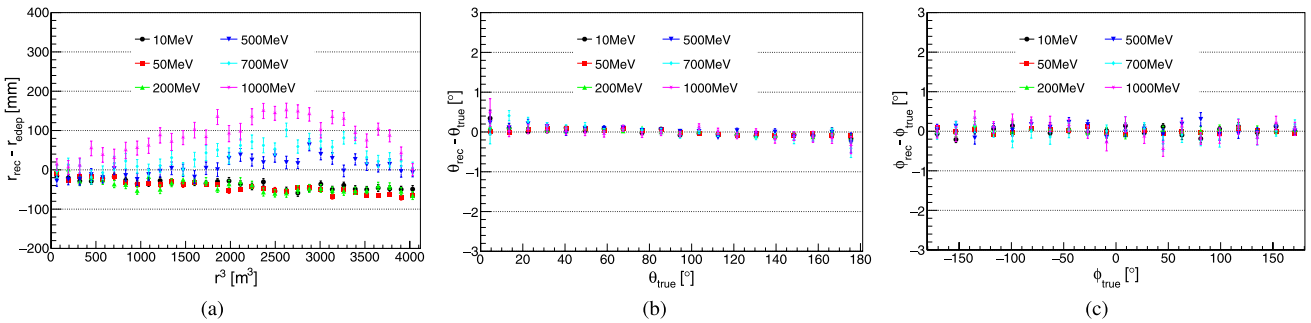

Fig. 15 Reconstruction bias of electron's energy-deposit center. **a** Reconstruction bias of r; **b** Reconstruction bias of θ direction; **c** Reconstruction bias of ϕ direction

from the data for algorithm performance verification, such as ^{12}B and Michel electrons. In addition, MC tuning is helpful for examining the various uncertainties that may arise from extrapolating low-energy events to high-energy events and estimating their potential impact.

5 Summary

Accurate energy reconstruction is crucial for detecting various physics events across a wide energy range, from MeV to GeV, in JUNO. This study proposes a unique method to reconstruct event energy using PMT counting technology, i.e., the OCCUPANCY method, which does not rely on precise charge measurements in a single PMT channel. Our reconstruction showed good performance in tests of the MC simulation samples. The energy nonuniformity can be controlled within 1% from the center of the detector to the edge for electrons with kinetic energies smaller than 500 MeV. As for 1 GeV electron, the energy nonuniformity can be controlled within 3%. The energy resolutions for 1 GeV electron FC events and FC+PC events were approximately 2.7% and 3.2%, respectively. This is the first demonstration of digital calorimetry using tens of thousands of PMTs in a large neutrino detector with potential applicability in current and future experiments employing similar detection techniques.

Acknowledgements We thank the JUNO reconstruction and simulation working group for many helpful discussions.

Author contributions All authors contributed to the study conception and design. Material preparation, data collection, and analysis were performed by Si-Yuan Zhang and Yong-Bo Huang. The first draft of the manuscript was written by Si-Yuan Zhang, Yong-Bo Huang, and Miao He, and all authors commented on previous versions of the manuscript. All authors read and approved the final manuscript.

Data availability The data that support the findings of this study are openly available in Science Data Bank at https://cstr.cn/31253.11.sciencedb.15335 and https://doi.org/10.57760/sciencedb.15335.

Declarations

Conflict of interest The authors declare that they have no Conflict of interest.

References

1. F.P. An, J.Z. Bai, A.B. Balantekin et al., Observation of electron-antineutrino disappearance at Daya Bay. Phys. Rev. Lett. **108**, 171803 (2012). https://doi.org/10.1103/PhysRevLett.108.171803
2. Y. Abe, C. Aberle, T. Akiri et al., Indication of reactor $\bar{\nu}_e$ disappearance in the double chooz experiment. Phys. Rev. Lett. **108**, 131801 (2012). https://doi.org/10.1103/PhysRevLett.108.131801
3. J.K. Ahn, S. Chebotaryov, J.H. Choi et al., Observation of reactor electron antineutrinos disappearance in the RENO experiment. Phys. Rev. Lett. **108**, 191802 (2012). https://doi.org/10.1103/PhysRevLett.108.191802
4. A. Gando, Y. Gando, H. Hanakago et al., Reactor on-off antineutrino measurement with KamLAND. Phys. Rev. D **88**, 033001 (2013). https://doi.org/10.1103/PhysRevD.88.033001
5. G. Bellini, J. Benziger, D. Bick et al., Neutrinos from the primary proton-proton fusion process in the Sun. Nature **512**, 383–386 (2014). https://doi.org/10.1038/nature13702
6. Y.F. Wang, S. Qian, T. Zhao et al., A new design of large area MCP-PMT for the next generation neutrino experiment. Nucl. Instrum. Meth. A **695**, 113–117 (2012). https://doi.org/10.1016/j.nima.2011.12.085
7. A. Abusleme, T. Adam, S. Ahmad et al., JUNO physics and detector. Prog. Part. Nucl. Phys. **123**, 103927 (2022). https://doi.org/10.1016/j.ppnp.2021.103927
8. M. He, Double calorimetry system in JUNO. Radiat. Detect. Technol. Methods **1**, 21 (2017). https://doi.org/10.1007/s41605-017-0022-2
9. C. Jollet, The 3-inch photomultiplier system of the JUNO experiment. PoS **ICHEP2020**, 203 (2021). https://doi.org/10.22323/1.390.0203
10. M. Ablikim, M.N. Achasov, S. Ahmed et al., Polarization and entanglement in baryon-antibaryon pair production in electron-positron annihilation. Nat. Phys. **15**, 631–634 (2019). https://doi.org/10.1038/s41567-019-0494-8
11. M. Ablikim, M.N. Achasov, P. Adlarson et al., Oscillating features in the electromagnetic structure of the neutron. Nat. Phys. **17**, 1200–1204 (2021). https://doi.org/10.1038/s41567-021-01345-6
12. W.J. Wu, M. He, X. Zhou et al., A new method of energy reconstruction for large spherical liquid scintillator detectors. JINST **14**, P03009 (2019). https://doi.org/10.1088/1748-0221/14/03/P03009
13. G.H. Huang, Y.F. Wang, W.M. Luo et al., Improving the energy uniformity for large liquid scintillator detectors. Nucl. Instrum. Meth. A **1001**, 165287 (2021). https://doi.org/10.1016/j.nima.2021.165287
14. G.H. Huang, W. Jiang, L.J. Wen et al., Data-driven simultaneous vertex and energy reconstruction for large liquid scintillator detectors. Nucl. Sci. Tech. **34**, 83 (2023). https://doi.org/10.1007/s41365-023-01240-0
15. Z. Qian, V. Belavin, V. Bokov et al., Vertex and energy reconstruction in JUNO with machine learning methods. Nucl. Instrum. Meth. A **1010**, 165527 (2021). https://doi.org/10.1016/j.nima.2021.165527
16. Z.Y. Li, Z. Qian, J.H. He et al., Improvement of machine learning-based vertex reconstruction for large liquid scintillator detectors with multiple types of PMTs. Nucl. Sci. Tech. **33**, 93 (2022). https://doi.org/10.1007/s41365-022-01078-y
17. A. Gavrikov, Y. Malyshkin, F. Ratnikov, Energy reconstruction for large liquid scintillator detectors with machine learning techniques: aggregated features approach. Eur. Phys. J. C **82**, 1021 (2022). https://doi.org/10.1140/epjc/s10052-022-11004-6
18. G. Settanta, S. Mari, C. Martellini *et al.*, Atmospheric neutrino spectrum reconstruction with JUNO. PoS **EPS-HEP2019**, 041 (2020). https://doi.org/10.22323/1.364.0041
19. A. Abusleme, T. Adam, S. Ahmad et al., JUNO sensitivity to low energy atmospheric neutrino spectra. Eur. Phys. J. C **81**, 10 (2021). https://doi.org/10.1140/epjc/s10052-021-09565-z
20. Z.K. Yang, J.X. Liu, H.Y. Duyang et al., First attempt of directionality reconstruction for atmospheric neutrinos in a large homogeneous liquid scintillator detector. Phys. Rev. D **109**, 052005 (2024). https://doi.org/10.1103/PhysRevD.109.052005

21. R. Wirth, M. Rifai, M.C. Molla et al., Reconstruction of atmospheric neutrino events at JUNO. PoS **ICHEP2022**, 1114 (2022). https://doi.org/10.22323/1.414.1114
22. M.C. Molla, M. Rifai, R. Wirth et al., Reconstruction of atmospheric neutrinos in JUNO. PoS **ICRC2023**, 1189 (2023). https://doi.org/10.22323/1.444.1189
23. F.P. An, G.P. An, Q. An et al., Neutrino physics with JUNO. J. Phys. G **43**, 030401 (2016). https://doi.org/10.1088/0954-3899/43/3/030401
24. A. Abusleme, T. Adam, S. Ahmad et al., Prospects for detecting the diffuse supernova neutrino background with JUNO. JCAP **10**, 033 (2022). https://doi.org/10.1088/1475-7516/2022/10/033
25. A. Abusleme, T. Adam, S. Ahmad et al., JUNO sensitivity on proton decay $p \to \bar{\nu}K^+$ searches. Chin. Phys. C **47**, 113002 (2023). https://doi.org/10.1088/1674-1137/ace9c6
26. C. Genster, M. Schever, L. Ludhova et al., Muon reconstruction with a geometrical model in JUNO. JINST **13**, T03003 (2018). https://doi.org/10.1088/1748-0221/13/03/T03003
27. K. Zhang, M. He, W.D. Li et al., Muon tracking with the fastest light in the JUNO central detector. Radiat. Detect. Technol. Methods **2**, 13 (2018). https://doi.org/10.1007/s41605-018-0040-8
28. Y. Liu, W.D. Li, T. Lin et al., Muon reconstruction with a convolutional neural network in the JUNO detector. Radiat. Detect. Technol. Methods **5**, 364–372 (2021). https://doi.org/10.1007/s41605-021-00259-4
29. C.F. Yang, Y.B. Huang, J.L. Xu et al., Reconstruction of a muon bundle in the JUNO central detector. Nucl. Sci. Tech. **33**, 59 (2022). https://doi.org/10.1007/s41365-022-01049-3
30. Z. Djurcic, V. Guarino, A. Cabrera et al., JUNO conceptual design report. https://doi.org/10.48550/arXiv.1508.07166
31. A. Abusleme, A. Abusleme, T. Adam et al., Sub-percent precision measurement of neutrino oscillation parameters with JUNO. Chin. Phys. C **46**, 123001 (2022). https://doi.org/10.1088/1674-1137/ac8bc9
32. Y.B. Huang, J.F. Chang, Y.P. Cheng et al., The Flash ADC system and PMT waveform reconstruction for the Daya Bay experiment. Nucl. Instrum. Meth. A **895**, 48–55 (2018). https://doi.org/10.1016/j.nima.2018.03.061
33. D. Adey, F.P. An, A.B. Balantek et al., A high precision calibration of the nonlinear energy response at Daya Bay. Nucl. Instrum. Meth. A **940**, 230–242 (2019). https://doi.org/10.1016/j.nima.2019.06.031
34. S. Blin, S. Callier, S.C. Di Lorenzo et al., Performance of CATIROC: ASIC for smart readout of large photomultiplier arrays. JINST **12**, C03041 (2017). https://doi.org/10.1088/1748-0221/12/03/C03041
35. S. Conforti, M. Settimo, C. Santos et al., CATIROC: an integrated chip for neutrino experiments using photomultiplier tubes. JINST **16**, P05010 (2021). https://doi.org/10.1088/1748-0221/16/05/P05010
36. T. Li, X. Xia, X.T. Huang et al., Design and development of JUNO event data model. Chin. Phys. C **41**, 066201 (2017). https://doi.org/10.1088/1674-1137/41/6/066201
37. K.J. Li, Z.Y. You, Y.M. Zhang et al., GDML based geometry management system for offline software in JUNO. Nucl. Instrum. Meth. A **908**, 43–48 (2018). https://doi.org/10.1016/j.nima.2018.08.008
38. T. Zhou, X.L. Ji, K.J. Zhu et al., DAQ readout prototype for JUNO. Radiat. Detect. Technol. Methods **5**, 600–608 (2021). https://doi.org/10.1007/s41605-021-00290-5
39. S. Zhang, J.S. Li, Y.J. Su et al., A method for sharing dynamic geometry information in studies on liquid-based detectors. Nucl. Sci. Tech. **32**, 21 (2021). https://doi.org/10.1007/s41365-021-00852-8
40. T. Lin, Y.X. Hu, M. Yu et al., Simulation software of the JUNO experiment. Eur. Phys. J. C **83**, 382 (2023). https://doi.org/10.1140/epjc/s10052-023-11514-x
41. S. Agostinelli, J. Allison, K. Amako et al., [GEANT4], GEANT4-a simulation toolkit. Nucl. Instrum. Meth. A **506**, 250–303 (2003). https://doi.org/10.1016/S0168-9002(03)01368-8
42. J. Allison, K. Amako, J. Apostolakis et al., Geant4 developments and applications. IEEE Trans. Nucl. Sci. **53**, 270 (2006). https://doi.org/10.1109/TNS.2006.869826
43. J. Allison, J. Apostolakis, S.B. Lee et al., Recent developments in Geant4. Nucl. Instrum. Meth. A **835**, 186–225 (2016). https://doi.org/10.1016/j.nima.2016.06.125
44. J.H. Zou, X.T. Huang, W.D. Li et al., SNiPER: an offline software framework for non-collider physics experiments. J. Phys. Conf. Ser. **664**, 072053 (2015). https://doi.org/10.1088/1742-6596/664/7/072053
45. X. Zhou, Q. Liu, M. Wurm et al., Rayleigh scattering of linear alkylbenzene in large liquid scintillator detectors. Rev. Sci. Instrum. **86**, 073310 (2015). https://doi.org/10.1063/1.4927458
46. L. Gao, B.X. Yu, Y.Y. Ding et al., Attenuation length measurements of a liquid scintillator with LabVIEW and reliability evaluation of the device. Chin. Phys. C **37**, 076001 (2013). https://doi.org/10.1088/1674-1137/37/7/076001
47. R. Zhang, D.W. Cao, C.W. Loh et al., Using monochromatic light to measure attenuation length of liquid scintillator solvent LAB. Nucl. Sci. Tech. **30**, 30 (2019). https://doi.org/10.1007/s41365-019-0542-1
48. M. Wurm, F. von Feilitzsch, M. Goeger-Neff et al., Optical scattering lengths in large liquid-scintillator neutrino detectors. Rev. Sci. Instrum. **81**, 53301 (2010). https://doi.org/10.1063/1.3397322
49. Y. Zhang, Z.Y. Yu, X.Y. Li et al., A complete optical model for liquid-scintillator detectors. Nucl. Instrum. Meth. A **967**, 163860 (2020). https://doi.org/10.1016/j.nima.2020.163860
50. X.F. Ding, L.J. Wen, X. Zhou et al., Measurement of the fluorescence quantum yield of bis-MSB. Chin. Phys. C **39**, 126001 (2015). https://doi.org/10.1088/1674-1137/39/12/126001
51. C. Buck, B. Gramlich, S. Wagner, Light propagation and fluorescence quantum yields in liquid scintillators. JINST **10**, P09007 (2015). https://doi.org/10.1088/1748-0221/10/09/P09007
52. H.M. O'Keeffe, E. O'Sullivan, M.C. Chen, Scintillation decay time and pulse shape discrimination in oxygenated and deoxygenated solutions of linear alkylbenzene for the SNO+ experiment. Nucl. Instrum. Meth. A **640**, 119–122 (2011). https://doi.org/10.1016/j.nima.2011.03.027
53. N. Li, Y.K. Heng, M. He et al., Characterization of 3-inch photomultiplier tubes for the JUNO central detector. Radiat. Detect. Technol. Methods **3**, 6 (2019). https://doi.org/10.1007/s41605-018-0085-8
54. C.Y. Cao, J.L. Xu, M. He et al., Mass production and characterization of 3-inch PMTs for the JUNO experiment. Nucl. Instrum. Meth. A **1005**, 165347 (2021). https://doi.org/10.1016/j.nima.2021.165347
55. J.W. Hardin, J.M. Hilbe, *Generalized linear models and extension* (Stata Press, USA, 2018)
56. A.Q. Zhang, B.D. Xu, J. Weng et al., Performance evaluation of the 8-inch MCP-PMT for Jinping Neutrino Experiment. Nucl. Instrum. Meth. A **1055**, 168506 (2023). https://doi.org/10.1016/j.nima.2023.168506
57. A. Abusleme, T. Adam, S. Ahmad et al., Calibration strategy of the JUNO experiment. JHEP **03**, 004 (2021). https://doi.org/10.1007/JHEP03(2021)004
58. D. Teng, J.L. Liu, G.L. Zhu et al., Low-radioactivity ultrasonic hydrophone used in positioning system for Jiangmen underground neutrino observatory. Nucl. Sci. Tech. **33**, 76 (2022). https://doi.org/10.1007/s41365-022-01059-1

59. H.R. Liu, Q.Q. Zhou, J.C. Liang *et al.*, Activity measurement of ^{55}Fe using the liquid scintillation TDCR method. Nuclear Techniques (in Chinese) **46**, 010501 (2023). https://doi.org/10.11889/j.0253-3219.2023.hjs.46.010501
60. R. Brun, F. Rademakers, ROOT: an object oriented data analysis framework. Nucl. Instrum. Meth. A **389**, 81–86 (1997). https://doi.org/10.1016/S0168-9002(97)00048-X
61. F. James, M. Roos, Minuit: a system for function minimization and analysis of the parameter errors and correlations. Comput. Phys. Commun. **10**, 343–367 (1975). https://doi.org/10.1016/0010-4655(75)90039-9
62. M. Hatlo, F. James, P. Mato et al., Developments of mathematical software libraries for the LHC experiments. IEEE Trans. Nucl. Sci. **52**, 2818–2822 (2005). https://doi.org/10.1109/TNS.2005.860152
63. Z.Y. Li, Y.M. Zhang, G.F. Cao et al., Event vertex and time reconstruction in large-volume liquid scintillator detectors. Nucl. Sci. Tech. **32**, 49 (2021). https://doi.org/10.1007/s41365-021-00885-z
64. M. Yu, L.J. Wen, X. Zhou et al., A universal energy response model for determining the energy nonlinearity and resolution of $e^{\pm}$ and γ in liquid scintillator detectors. Eur. Phys. J. C **83**, 403 (2023). https://doi.org/10.1140/epjc/s10052-023-11541-8